Research Square

Preprints are preliminary reports that have not undergone peer review.
They should not be considered conclusive, used to inform clinical practice,
or referenced by the media as validated information.

Decoding Metal Cluster Stability and Evolution via a Geometry-Confined Superatomic Shell Model

Zhixun Luo

zxluo@iccas.ac.cn

Institute of Chemistry Chinese Academy of Sciences https://orcid.org/0000-0002-5752-1996

Qiuying Du

Institute of Chemistry Chinese Academy of Sciences

Weizhe Wang

Institute of Chemistry Chinese Academy of Sciences

Shiquan Lin

Institute of Chemistry Chinese Academy of Sciences

Jijun Zhao

South China Normal University

S Khanna

Virginia Commonwealth University https://orcid.org/0000-0002-9797-1289

Article

Keywords:

Posted Date: October 28th, 2026

DOI: https://doi.org/10.21203/rs.3.rs-11262953/v1

License: This work is licensed under a Creative Commons Attribution 4.0 International License.
Read Full License

Additional Declarations: There is **NO** Competing Interest.

Decoding Metal Cluster Stability and Evolution via a Geometry-Confined Superatomic Shell Model

Qiuying Du[1,3,ξ], Weizhe Wang[1,2,ξ], Shiquan Lin[1,2], Jijun Zhao[4], Shiv N. Khanna[5], Zhixun Luo[1,2*]

[1]Beijing National Laboratory for Molecular Sciences (BNLMS), State Key Laboratory for Structural Chemistry of Unstable and Stable Species, Institute of Chemistry, Chinese Academy of Sciences; Beijing 100190, China.

[2]School of Chemistry, University of Chinese Academy of Sciences; Beijing 100049, China.

[3]College of Physics and Electronic Information, Inner Mongolia Key Laboratory of Applied Condensed Matter Physics, Inner Mongolia Normal University; Hohhot 010022, China.

[4]Guangdong Provincial Key Laboratory of Quantum Engineering and Quantum Materials, School of Physics, South China Normal University; Guangzhou 510006, China.

[5]Department of Physics, Virginia Commonwealth University; Richmond, VA 23284-2000, USA.

*Corresponding author. Email: zxluo@iccas.ac.cn

[ξ] These authors contributed equally to this work.

Atomic clusters represent the miniaturization limit of nanoparticles, where quantum size effects and discrete energy levels govern their properties. Classical jellium model and Clemenger-Nilsson model have well explained electronic shell structures of metal clusters, enabling the prediction of magic numbers; however, they struggle for low-symmetry or ligated systems. Here we prepare well-resolved gold clusters, examine their reactivities, and find that Au_{13}^- and $Au_{14}NO^-$ exhibit prominent inertness, which deviates from the predicted shell closures based on the common models. We introduce a geometry-confined superatomic shell (GCSS) model, through which we elucidate the enhanced stability of Au_{13}^- pertaining to superatomic orbital splitting and subshell closure ($1S^2|1P^4|1P^2|1D^6||1D^0|$). We demonstrate Au_{14}^- as a near-critical cluster with labile frontier orbitals, allowing for superatomic orbital level reordering and enhanced stability in forming $Au_{14}NO^-$. Utilizing this GCSS model, we elucidate the size-dependent stability and reactivity of gold clusters, extending superatomic engineering from the spherical jellium model to geometry-confined superatomic shells that incorporate both geometric and ligand effects.

Subnanometer metal clusters—comprising a few to several tens of atoms—define the ultimate miniaturization limit of metals, where every atom and electron governs the overall property[1,2]. Unlike bulk metals, these clusters display discrete energy levels, quantum size effects, and atom-mimicking orbitals with enhanced stability at magic numbers[3-7], bridging the gap between isolated atoms and nanoparticles[8-10]. The well-established nearly-free electron gas (NFEG) theory and jellium model, built on solving the Schrödinger equation within spherical harmonic oscillator, square-well, or Woods–Saxon potentials[11-13], have predicted diverse magic numbers (e.g., 2, 8, 18,

20, 34, 40, 58, …) across different metal clusters[14-16]. The Clemenger–Nilsson model further introduced ellipsoidal deformation to explain shell splitting in metal clusters[17,18], and a recent symmetry-adapted orbital (SAO) model extended this to I_h, O_h, and T_d symmetries, showing orbital splitting and inverted 2S/1D ordering under T_d symmetry[19,20]. But these frameworks encounter difficulties with clusters lacking distinct symmetry, as well as those containing heteroatoms or ligands, thereby leaving a need for a unified model based on shape-confined potentials[21-23].

Coinage metal clusters, particularly gold[24,25], provide a stringent testing ground owing to strong relativistic effects and *s–d* hybridization that drive rich structural diversity—from planar (Au_{1-11}^-) to bilayer/oblate (Au_{12-15}^-), hollow-cage (Au_{16}^- and Au_{17}^-), core–shell (Au_{18}^-), and tetrahedral (Au_{19-20}^-) motifs. However, a few key questions remain unsolved, including the origin of 2D-to-3D transition[26] and the magic numbers of gold clusters[27,28], and the relative stability of Au_{13}^- versus Au_{17}^-. Notably, small gold clusters are prone to oxygen contamination and undergo complex structural evolution[29,30]; also, reliable metal cluster experiments demands stringent local pressure conditions and a fine balance between cluster growth driven by gas condensation and dynamic dissociation induced by gas collisions. To date, a normal Gaussian distribution of pure gold cluster anions has rarely been reported, which substantially hinders a fair comparison of their size-dependent stability and reactivity.

Here we address these questions by integrating a geometry-confined superatomic shell (GCSS) model with self-consistent DFT calculations, combining with mass spectrometry experiments. We prepared well-resolved gold clusters and performed a rigorous comparative analysis of their size-dependent reactivity. Through a joint experimental and theoretical study, we elucidate the origin of unique stability of Au_{13}^- and identify Au_{14}^- as a near-critical cluster with perturbation-sensitive frontier orbitals and its NO binding populates a superatomic 1F state. We further elucidate the structural evolution of bare Au_n^- clusters arising from competing shell-ordering tendencies governed by size and shape, and demonstrate the reactivity of Au_n^- with O_2 and NO, thereby validating the GCSS model that extends beyond spherical jellium and offers a route to engineer superatomic states in metal clusters[31,32].

Results and discussion

Mass spectrometry

Gold clusters Au_n^- (n = 7–21) were generated via laser vaporization (15–20 mJ, 532 nm) of a gold target disk (99.999% purity, Φ = 16 × 3 mm), carried by pulsed helium gas flow (99.999%, 10 atm) through a tube nozzle (Φ = 2 mm, L = 35 mm), and then analysed using a home-built high-resolution reflection time-of-flight mass spectrometer (Re-TOFMS)[33]. We prepared pure gold clusters (free of contamination) with a normal Gaussian distribution to fairly compare their size-dependent stability and reactivity, as shown in Fig. 1A-a. The down-stream reactions with oxygen (5% in He, 1 atm) were controlled by adjusting the pulse valve width, yielding $Au_nO_2^-$ products with varying reaction conditions. As shown in Fig. 1A, the even-numbered gold clusters (except Au_{10}^- and Au_{16}^- within unique geometry)[34] are very reactive with oxygen, whereas the odd-numbered ones are largely unreactive, especially Au_{13}^-. This trend is consistent with the previously published studies of Ag_n^- and Cu_n^- clusters[29,35,36]. The odd-even oscillating reactivity of Au_n^- arises from their shell structures[37-41] and alternately filled and half-filled sub-shells[42]. The even-number Au_n^- clusters feature lower electron detachment energies and facilitate electron transfer from gold to oxygen[43]. This odd-even effect and prominent inertness of Au_{13}^- were repeatedly observed in the gas-phase reaction experiments (Supplementary Figs. 1 and 2), indicating its unusual stability.

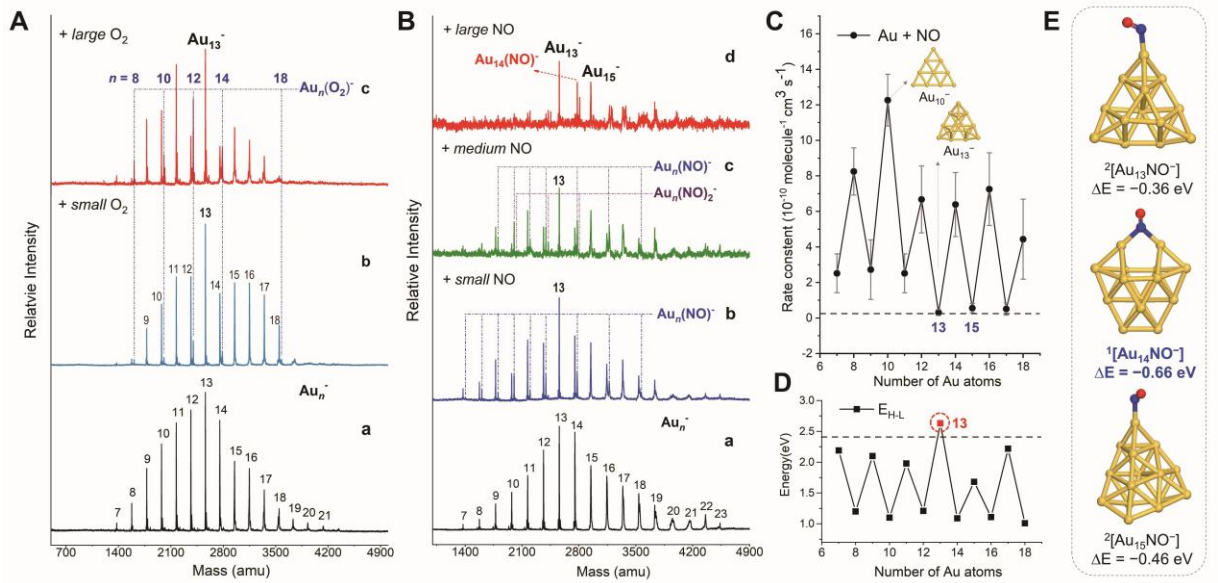


Fig. 1 | Au_n^- reacting with O_2 and NO. A, Mass spectra of the Au_n^- (n = 7–21) clusters produced by a homemade Lava source, in the absence (**a**) and presence (**b-c**) of different doses of oxygen reactant (5% in He, 1 atm). The oxygen reactant of small (**b**) and large (**c**) doses correspond to pulsed (10 Hz) widths at 190 μs and 215 μs respectively. **B**, Mass spectra of the Au_n^- (n = 7−23) clusters reacting with different amounts of nitrogen monoxide (5% in He, 1 atm). The small (**b**), medium (**c**), and large (**d**) doses of the reactant correspond to pulsed (10 Hz) widths at 190 μs, 210 μs, and 230 μs, respectively. **C**, The estimated quasi first-order reaction rate constants for Au_n^- clusters with NO. The insets show the $Au_{10,13}^-$ cluster structures. **D**, DFT-calculated HOMO–LUMO gaps (E_{H-L}) of the Au_n^- clusters at the PBE0/SDD level of theory. **E**, Adsorption energies (ΔE), structures, and spin multiplicities of NO on the Au_{13-15}^- clusters, calculated at the revTPSS/SDD level of theory.

Structure chemistry analysis

Through a global-minima search utilizing an unbiased comprehensive genetic algorithm (CGA)[44] and subsequent re-optimization with Gaussian 16 software[45], we have determined the lowest energy structures of the Au_n^- clusters and their reaction products (Supplementary Figs. 6–11). The geometric structures of these gold clusters are consistent with the previous studies[43]. Notably, the adsorption of O_2 on the odd-number gold clusters (even number of electrons) prefers a triplet state (except Au_{19}^-), with small O_2-binding energies of less than 0.1 eV (Supplementary Fig. 12). This may account for the lack of oxide products for the odd-numbered Au_n^- clusters. Natural charge population analysis (NPA) and spin density distribution (Supplementary Tables 1 and 2) indicate that the reactions of even-numbered Au_n^- clusters with oxygen are associated with electron transfer processes, namely, partial charges transferred from gold to the O_2 molecule. Without forming dissociative oxygen-bridge species, or superoxo/peroxo intermediates[46], the end-on and side-on adsorption of O_2 on all these gold cluster anions induces relatively weak charge transfer with a magnitude of no more than 1.0 |e|.

To further explore the intrinsic properties of size-dependent Au_n^- clusters, we have also studied the reactions of Au_n^- clusters with NO, as shown in Fig. 1B. In contrast to O_2 which requires gold clusters to act as electron donors during reaction, NO can act as either an electron donor or an acceptor because it contains an unpaired electron in its antibonding π* orbital[47,48]. In the formation of the $Au_n(NO)^-$ products, the unpaired antibonding π* electron of NO becomes delocalized over the gold cluster, resulting in balanced nucleus-electron interactions and additional stabilization

energy. This stabilization energy is associated with electron delocalization and superatom-based bonding, mimicking conjugation stabilization in aromatic molecules which can be quantified within the Hückel molecular orbital framework. At a relatively low concentration of the NO reactant (e.g., a pulse width of 190 μs), distinct NO adducts were found for the Au_n^- (n = 7, 9, 11) clusters, alongside rapid reactivity observed for even-sized ones; in comparison, the larger odd-number Au_n^- (n = 13, 15, 17, 19) clusters barely form detectable adduct products.

With the elevation of NO concentration, several reaction products of $Au_n(NO)_2^-$ were detected, showing successive reaction and favourable addition of one or two NO molecules. However, even when exposed to a large amount of NO reactant, Au_{13}^- and Au_{15}^- do not attach any NO molecules, and Au_{13}^- shows greater inertness than Au_{15}^- (see Supplementary Figs. 3 and 4 for further details). This aligns with the previous finding of relative inertness of Ag_{13}^- than Ag_{15}^- (ref.[42]). Reaction rate constant calculations (Fig. 1C) validate the exceptional inertness of Au_{13}^- among all the studied Au_n^- clusters (for oxygen-reaction rates, see Supplementary Fig. 5). This coincides remarkably with the largest HOMO−LUMO gap of Au_{13}^- among the studied clusters (Fig. 1D). The exceptional stability of Au_{13}^- is also associated with its low electron affinity and large electron detachment energy, as well as strong second-order binding energy (Supplementary Fig. 13 and Tables 3 and 4). For even-sized clusters, Au_{14}^- behaves differently from the others and solely forms $Au_{14}NO^-$ even at high NO concentrations. Both Au_{10}^- and Au_{16}^- show considerable reactivity with NO, and Au_{10}^- shows the overall fastest reaction rate. The reaction trends observed in Fig. 1B are consistently reproduced across repeated experiments (Supplementary Figs. 3 and 4).

We compared the NO adsorption energies on these clusters (Fig. 1E, Supplementary Figs. 11 and 12), and find that Au_{13}^- exhibits the lowest adsorption energy among all the studied Au_n^- clusters, whereas Au_{10}^- shows the highest value. Apart from this, the open-shell superatom clusters possess higher reactivity than closed-shell counterparts. Notably, the reactions of Au_8^-, Au_{12}^-, Au_{18}^-, and Au_{20}^- all lead to Au_nNO^- products of a triplet spin state, with spin density largely localized on the NO moiety. This feature suggests weak orbital coupling interactions between gold cluster anions and NO molecules (Supplementary Table 2 and Fig. 14). Likewise, the NO adsorption products of odd-sized clusters favour a doublet state, where spin density is predominantly centred on NO, pointing to feeble Au-NO interactions (Supplementary Table 2). In contrast, $Au_{10}NO^-$, $Au_{14}NO^-$, and $Au_{16}NO^-$ each adopt a singlet state, reflecting orbital hybridization between the gold cluster and NO (Supplementary Fig. 15). Overall, the adsorption behaviour of NO on Au_n^- clusters is closely correlated with the valence electrons of the cluster, as well as the orbital matching between the cluster and the NO molecule.

Quantum chemistry analysis

Fig. 2 compares the partial densities of states (PDOS) and superatomic orbitals of Au_{13}^-, Au_{14}^-, and $Au_{14}NO^-$ clusters (more details in Supplementary Figs. 16–24). The superatomic states of these clusters feature low-lying 1S orbitals and vivid 1P and 1D orbitals. The PDOS results reveal that the deep valence region below −8 eV is governed by Au-*s* orbital contributions, while the frontier orbitals indicate a mixing of Au-*s*, Au-*p*, and Au-*d* orbitals, originating from strong relativistic effects of Au atoms. Of particular interest, Au_{13}^- splits the 1D manifold and produces a HOMO-LUMO gap of 2.63 eV despite the absence of a spherical shell closure. Adding one atom and one valence electron gives an open-shell Au_{14}^- which shows a smaller HOMO-LUMO gap of 1.09 eV. Upon NO incorporation, the HOMO/LUMO levels shift from its initial orbital level $1D_{yz}/1D_{xz}$ to $1F_{y(3x^2-y^2)}/1F_{z^3}$, accompanied by a noticeable increase of the HOMO–LUMO

gap (2.0 eV). Charge decomposition analysis (CDA) (Supplementary Fig. 25) shows that the superatomic $1F_{y(3x^2-y^2)}$ orbital is symmetry-matched to the NO π* orbital, strengthening Au_{14}^--to-NO back-donation interaction. The distinct superatomic orbitals in Au_{13}^- and $Au_{14}NO^-$ clusters help balance their nuclear-electron interactions, thereby enhancing cluster stability, consistent with the experimentally observed inertness. Notably, these gold clusters exhibit superatomic orbital level splitting, shifting, and reordering, which deviates from the simple shell closure predicted by the spherical jellium or Clemenger-Nilsson shell models.

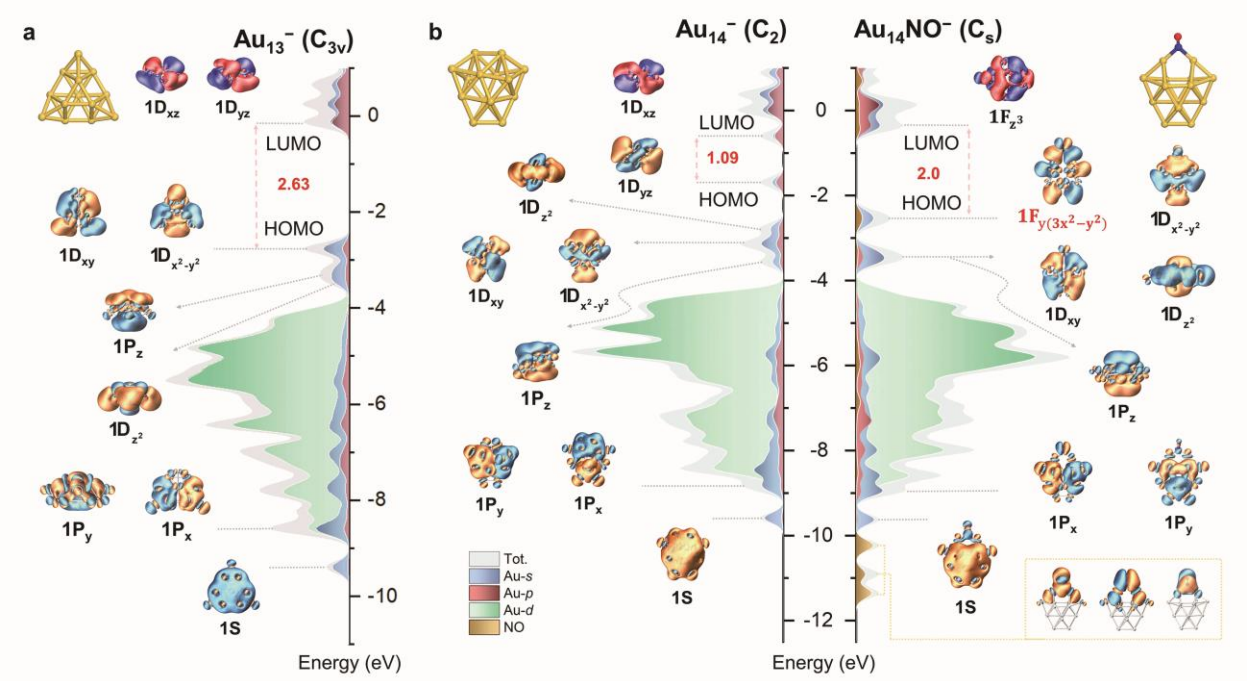


Fig. 2 | Electronic properties of $Au_{13,14}^-$ and $Au_{14}NO^-$. a–b, Partial densities of states (PDOS) and superatomic orbitals for the Au_{13}^-, Au_{14}^-, and $Au_{14}NO^-$ clusters, respectively, calculated at the PBE0/SDD level of theory. The light grey shaded area donates the total density of states (TDOS), whereas the blue, red, green and orange curves represent the PDOS contributions from the Au *s*, *p*, *d* and NO orbitals, respectively. Unless otherwise noted, an isovalue of 0.01 a.u. is used throughout this work. For the occupied orbitals, orange and light blue patterns denote the positive and negative phases of the wavefunctions respectively; red and blue denote the positive and negative phases of the wavefunction for unoccupied orbitals, respectively.

GCSS model investigations

To fully unveil the unusual stability of Au_{13}^- and $Au_{14}NO^-$ clusters, we propose a GCSS model to rationalize the delocalized electrons in such clusters having nonspherical structures, as shown in Fig. 3. This GCSS model incorporates particle confinement in arbitrary infinite potential wells, including triangular, circular, square, triangular-prismatic, triangular-pyramidal, spherical, tetrahedral, cuboctahedral, and ellipsoidal wells, as well as user-defined geometries with confining regions given by electron-density isosurfaces (for details, see Supplementary Figs. 26–30). We assume the potential barrier is sufficiently high such that the electron tunnelling probability is nearly zero and electron escape can be neglected. Thus, each delocalized electron as an independent particle confined to a domain Ω can be solved via the stationary Schrödinger equation.

The domain Ω is defined either by an analytical geometry rasterized by an interior-exterior mask, or directly from a DFT electron-density cube (for details see Supplementary text).

Based on the GCSS modelling calculations, the enhanced stability of Au_{13}^- and $Au_{14}NO^-$ is re-examined with the electron-density surfaces directly as the GCSS boundaries (Fig. 4). The C_{3v}-symmetric double-layer Au_{13}^- denotes a 14-electron configuration, giving rise to superatomic 1D splitting and a subshell closure ($1S^2|1P^4|1P^2|1D^6||1D^0|$) with a very large gap of 2.9 E* (where E* denotes the dimensionless energy unit of the GCSS; see Supplementary text). Within the GCSS model, the Au_{14}^- exhibits a superatomic open-shell electron configuration ($1S^2|1P^4|1P^2|1D^6|1D^1$). Upon NO incorporation, the confining potential becomes more oblate and induces superatomic 1D splitting and 1F descending, yielding a 16-electron configuration ($1S^2|1P^4|1P^2 1D^2|1D^4|1F^2||1D^0$). Similarly, we also studied the heteroatom-doped clusters such as I_h-symmetric Mo@Au_{12} and O_h-symmetric Sc@Au_{12}^+, as well as a ligand-protected $[Au_{13}]^{5+}$ nanocluster. For all these systems, the ordering of superatomic orbital levels and the corresponding electron-cloud patterns closely match the DFT calculation results. This agreement validates a broad applicability of the GCSS model and demonstrates that the boundary shape effectively accounts for the primary influence of structural rearrangement on the low-energy superatomic states.

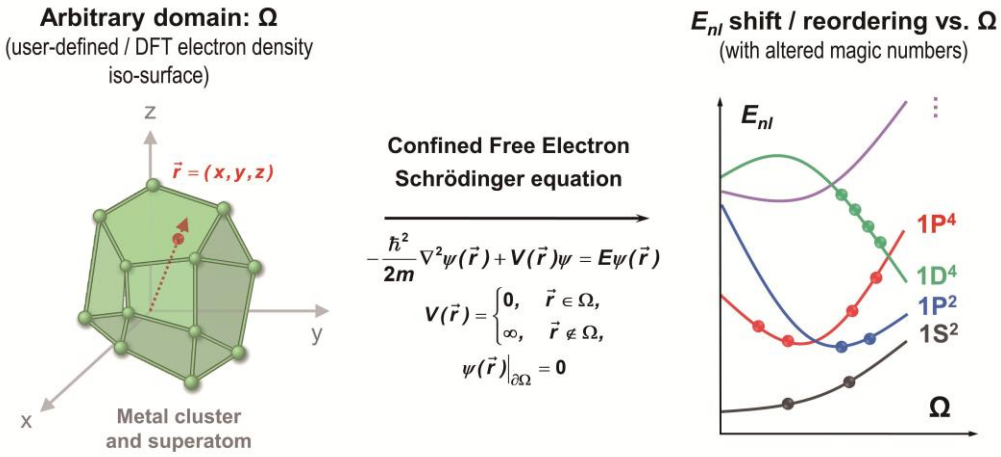


Fig. 3 | Schematic illustration and typical results of the geometry-confined superatomic shell (GCSS) model. The electron confinement region is represented by an arbitrary potential domain Ω, defined either by a user-specified geometry or by electron-density isosurface obtained from DFT calculations. Within Ω, electrons are treated as confined free electrons, whereas an infinite potential barrier is imposed outside the domain. The boundary of the confinement potential is denoted as ∂Ω, where the wavefunction satisfies the boundary condition $\psi(\vec{r})|_{\partial\Omega} = 0$. Solving the Schrödinger equation under different confinement geometries reveals that the superatomic energy levels E_{nl} are determined by the shape and size of Ω, rendering orbital energy shifts, level reordering, and altered magic numbers.

The same principle extends beyond the gold clusters. Across oblate, prolate, triangular-prismatic and triangular-pyramidal domains, the GCSS modelling calculations (Fig. 5) reproduce the results of first-principles calculations, seen as superatomic orbital level ordering, symmetry-resolved splitting and degeneracy patterns for the naked, doped and ligand-passivated M_nX_m clusters (M = Na, Mg, Al, Cu, Ag, Au, Bi, Sn; X = Sc, Mo, Cl, I, NO) (Supplementary Figs. 31–35, and Supplementary Tables 5–9). These comparisons reveal a shape-dependent interpretation of electronic magic numbers. Each confining geometry produces a distinct orbital sequence and a

set of shell-closing conditions, with the electron count determining which levels are occupied. The GCSS framework thus enables two complementary types of prediction: for a specified cluster, it can estimate the electron number required to produce subshell closures; for a fixed electron count, it helps to evaluate shapes, dopants, or ligands that promote shell closure. In view of this, the confining potential and the electron count operate as a coupled control mechanism governing both magic-number behaviour and the properties of delocalized electrons.

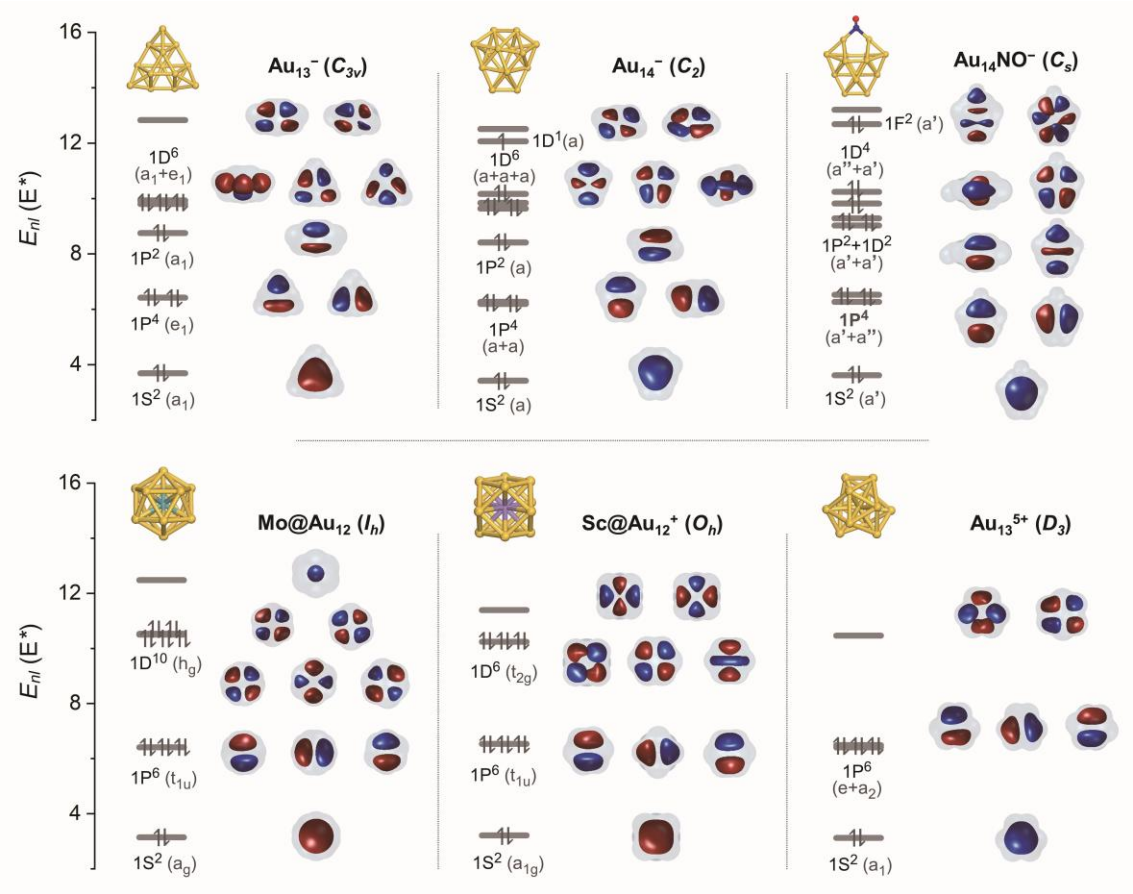


Fig. 4 | Simplified free-electron orbital energy levels based on the GCSS modelling calculations. Red and blue denote the positive and negative phases of the correlative wavefunction, respectively. The corresponding energy values under equal-volume scaling (E*) and a comparison with that given by units of electron volts (eV) are provided in Supplementary Fig. 30 and Supplementary Table 10.

Taken together, the GCSS model leads to three general conclusions. First, spherical geometries are not always energetically favourable for metal clusters, which allow superatomic states to balance nucleus-electron interactions and delocalized electrons with additional stabilization energy. By reshaping the confining domain, a cluster can tune the splitting and reordering of superatomic orbital levels and thereby open an energy gap larger than that in a spherical potential, as illustrated by oblate Au_{13}^-, triangular prism $[Au_{10}]^{2-}$, and tetrahedral Au_{20} (Fig. 5, Supplementary Fig. 29, and Supplementary Table 10). Second, within this GCSS framework, the electronic magic numbers are not restricted to conventional jellium shell closures but can include 6, 8, 10, 12, 14, 16, 18, 20, 24, 26, 28, 34, 40, etc. Third, the GCSS model facilitates the rational design of superatomic clusters by allowing geometric confinement, dopants, and ligands to modify

the cluster potential, thereby providing targeted control over orbital ordering and magic numbers. In light of this, geometric confinement is not simply a structural outcome but rather a tuneable variable that dictates electronic shell structure, superatomic states, and orbital level sequences[49].

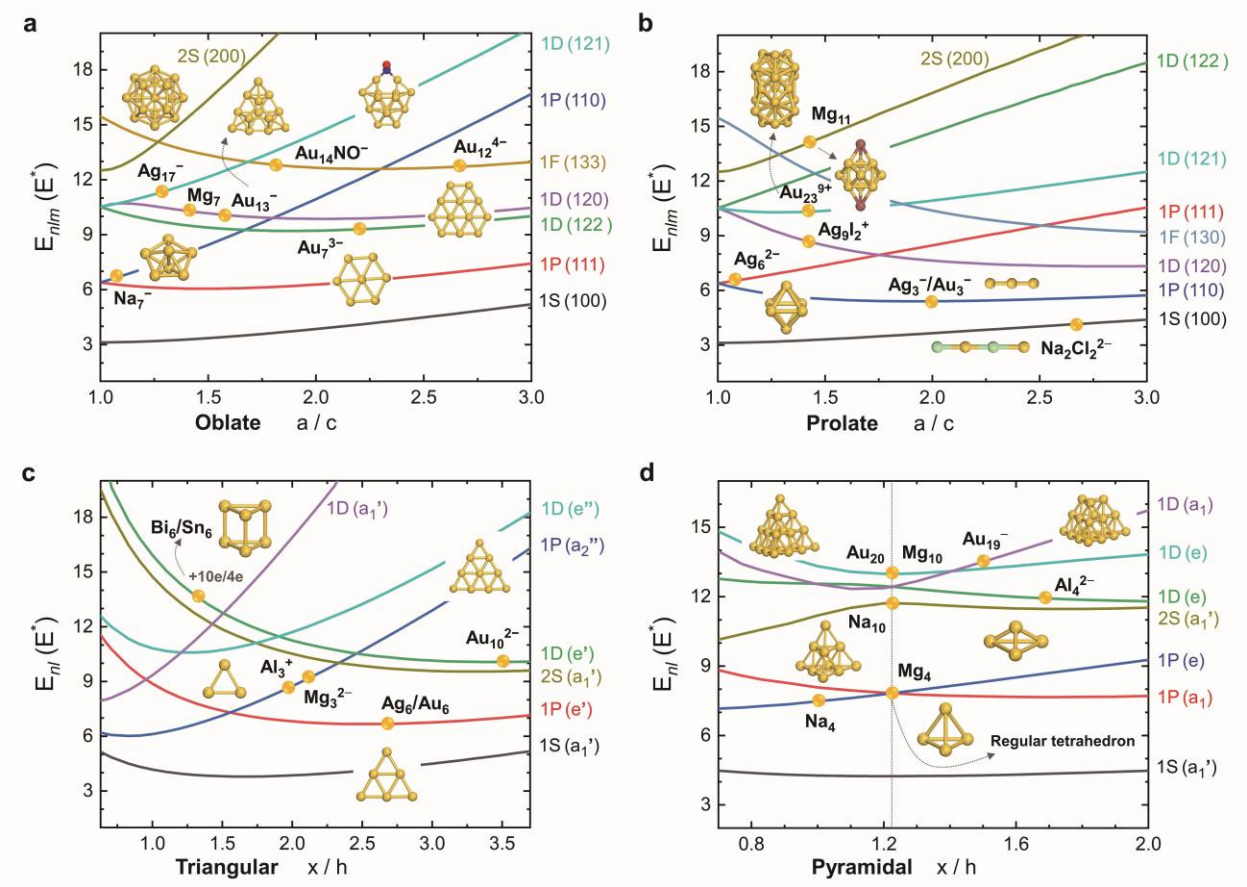


Fig. 5 | Application of the GCSS model. a–d, Schematic illustration of the GCSS model for typical metal clusters and superatoms at varied deformation ratios *a/c* or *x/h* of the oblate (**a**), prolate (**b**), regular triangular prism (**c**) and regular triangular pyramid (**d**) potential domains. For both oblate and prolate, the *a* and *c* donate the semi-major and semi-minor axes, respectively. For both the regular triangular prism and the regular triangular pyramid, the *x* and *h* donate the base side length and the height, respectively.

Conclusions

In summary, we combine geometry-confined superatomic shell model, density functional theory calculations, and gas-phase mass spectrometry to investigate the stability and reactivity of pure metal clusters Au_n^- (n = 1–20). Apart from the odd-even alternation in reactivity with O_2, our results demonstrate remarkable inertness of Au_{13}^-, pertaining to its unique electronic configuration and large HOMO–LUMO gap, as well as low O_2 adsorption energy. Reactivity studies with NO further confirm the stability of Au_{13}^-, and identify Au_{14}^- as a near-critical cluster, where NO adsorption induces substantial structural rearrangement that stabilizes its superatomic 1F orbital and widens its HOMO–LUMO gap. Furthermore, we propose a GCSS model that incorporates particle confinement in both 2D and 3D infinite potential wells of variable geometry. This model rationalizes orbital level splitting, mixing, and reordering by establishing the shape of the confining potential as a key determinant of both geometric and electronic structural evolution. Also, it helps

clarify the long-standing question of why M_{13}^- (M = Cu, Ag, Au) exhibits stability comparable to that of the magic-number cluster M_{17}^-. Apart from the insights into the small coinage metal clusters, this GCSS model is also applicable to larger clusters and other metals, as well as heteroatom-doped or ligand-stabilized systems. These findings advance our understanding of superatomic features in metal clusters, shed light on cluster stability and structure evolution mechanisms, and validate the strategy for tuning superatomic states via heteroatom doping or ligand effects—expanding the prospects for superatom engineering in catalysis, materials design, and nanotechnology.

Acknowledgments

We thank Prof. Longjiu Cheng for his friendly communication. We also acknowledge the use of OpenAI for debugging MATLAB scripts in this study. This work was supported by the National Natural Science Foundation of China (Grant No. 92261113, 12304298), CAS Project for Young Scientists in Basic Research (Grant No. YSBR-050), and Beijing Natural Science Foundation (F251006).

Author contributions

Z.L. conceived and supervised the research project. Q. D. conducted the theoretical calculations and organized the results. W.W. and S.L. conducted the experiments. All authors contributed to writing and revising the manuscript.

Competing interests

The authors declare no competing interests.

Additional information

Supplementary information is available for this paper at https://doi.org/10.***.

All experimental and computational details are provided in the supplementary materials.

Data availability

All data generated or analysed during this study are included in this published article and its supplementary information files.

Code availability

The MATLAB scripts developed for the GCSS modelling analysis are available at Zenodo (DOI: 10.5281/zenodo.22127728).

References

1. Castleman, A. W., Jr., Keesee, R. G. Clusters: Bridging the gas and condensed phases. *Acc. Chem. Res.* **19**, 413−419 (1986).
2. Moskovits, M. Metal clusters. *Annu. Rev. Phys. Chem.* **42**, 465−499 (1991).

3. Knight, W. D., Clemenger, K., de Heer, W. A., Saunders, W. A., Chou, M. Y., Cohen, M. L. Electronic shell structure and abundances of sodium clusters. *Phys. Rev. Lett.* **52**, 2141−2143 (1984).
4. De Heer, W. A. The physics of simple metal-clusters - experimental aspects and simple-models. *Rev. Mod. Phys.* **65**, 611−676 (1993).
5. Luo, Z., Castleman, A. W., Jr. Special and general superatoms. *Acc. Chem. Res.* **47**, 2931−2940 (2014).
6. Reber, A. C., Khanna, S. N. Superatoms: Electronic and geometric effects on reactivity. *Acc. Chem. Res.* **50**, 255−263 (2017).
7. Jena, P., Sun, Q. Super atomic clusters: Design rules and potential for building blocks of materials. *Chem. Rev.* **118**, 5755−5780 (2018).
8. Halperin, W. P. Quantum size effects in metal particles. *Rev. Mod. Phys.* **58**, 533−606 (1986).
9. Koutecky, J., Fantucci, P. Theoretical aspects of metal atom clusters. *Chem. Rev.* **86**, 539−587 (1986).
10. Khanna, S. N., Jena, P. Atomic clusters: Building blocks for a class of solids. *Phys. Rev. B* **51**, 13705−13716 (1995).
11. Ekardt, W. Dynamical polarizability of small metal particles: Self-consistent spherical jellium background model. *Phys. Rev. Lett.* **52**, 1925−1928 (1984).
12. Nishioka, H., Hansen, K., Mottelson, B. R. Supershells in metal clusters. *Phys. Rev. B* **42**, 9377−9386 (1990).
13. Brack, M. The physics of simple metal clusters: Self-consistent jellium model and semiclassical approaches. *Rev. Mod. Phys.* **65**, 677−732 (1993).
14. Leuchtner, R. E., Harms, A. C., Castleman, A. W. Thermal metal cluster anion reactions - behavior of aluminum clusters with oxygen. *J. Chem. Phys.* **91**, 2753−2754 (1989).
15. Alameddin, G., Hunter, J., Cameron, D., Kappes, M. M. Electronic and geometric structure in silver clusters. *Chem. Phys. Lett.* **192**, 122-128 (1992).
16. Bergeron, D. E., Castleman, A. W., Morisato, T., Khanna, S. N. Formation of $Al_{13}I^-$: Evidence for the superhalogen character of Al_{13}. *Science* **304**, 84−87 (2004).
17. Clemenger, K. Ellipsoidal shell structure in free-electron metal clusters. *Phys. Rev. B* **32**, 1359−1362 (1985).
18. Magaud, L., Khanna, S. N., Jena, P. Limitation on the success of the jellium model for metal clusters. *Chem. Phys. Lett.* **183**, 333−336 (1991).
19. Haruta, N., Tsukamoto, T., Kuzume, A., Kambe, T., Yamamoto, K. Nanomaterials design for super-degenerate electronic state beyond the limit of geometrical symmetry. *Nat. Commun.* **9**, 3758 (2018).
20. Tsukamoto, T., Haruta, N., Kambe, T., Kuzume, A., Yamamoto, K. Periodicity of molecular clusters based on symmetry-adapted orbital model. *Nat. Commun.* **10**, 3727 (2019).
21. Medel, V. M., Reveles, J. U., Khanna, S. N., Chauhan, V., Sen, P., Castleman, A. W. Hund's rule in superatoms with transition metal impurities. *Proc. Natl. Acad. Sci. U. S. A.* **108**, 10062−10066 (2011).
22. Luo, Z., Khanna, S. *Metal clusters and their reactivity*. Springer: Springer Nature Singapore Pte Ltd., 2020.
23. Jena, P., Sun, Q. *Superatoms ——principles, synthesis and applications*. John Wiley & Sons Ltd, 2022.
24. Huang, W., Ji, M., Dong, C. D., Gu, X., Wang, L. M., Gong, X. G.*, et al.* Relativistic effects and the unique low-symmetry structures of gold nanoclusters. *ACS Nano* **2**, 897−904 (2008).
25. Yin, B., Luo, Z. Coinage metal clusters: From superatom chemistry to genetic materials. *Coord. Chem. Rev.* **429**, 213643 (2021).
26. Huang, W., Wang, L.-S. Probing the 2d to 3d structural transition in gold cluster anions using argon tagging. *Phys. Rev. Lett.* **102**, 153401 (2009).
27. Li, J., Li, X., Zhai, H. J., Wang, L. S. Au_{20}: A tetrahedral cluster. *Science* **299**, 864−867 (2003).
28. Gruene, P., Rayner, D. M., Redlich, B., van der Meer, A. F. G., Lyon, J. T., Meijer, G.*, et al.* Structures of neutral Au_7, Au_{19}, and Au_{20} clusters in the gas phase. *Science* **321**, 674−676 (2008).
29. Stolcic, D., Fischer, M., Gantefor, G., Kim, Y. D., Sun, Q., Jena, P. Direct observation of key reaction intermediates on gold clusters. *J. Am. Chem. Soc.* **125**, 2848−2849 (2003).
30. Ma, J., Cao, X., Chen, M., Yin, B., Xing, X., Wang, X. Low-temperature disproportionation reaction of NO on Au_6^-: A mechanism involving three NO molecules promoted by the negative charge. *J. Phys. Chem. A* **120**, 9131–9137 (2016).
31. Walter, M., Akola, J., Lopez-Acevedo, O., Jadzinsky, P. D., Calero, G., Ackerson, C. J.*, et al.* A unified view of ligand-protected gold clusters as superatom complexes. *Proc. Natl. Acad. Sci. U. S. A.* **105**, 9157−9162 (2008).
32. Omoda, T., Takano, S., Tsukuda, T. Toward controlling the electronic structures of chemically modified superatoms of gold and silver. *Small* **17**, 2001439 (2021).
33. Zhang, H., Wu, H., Jia, Y., Geng, L., Luo, Z., Fu, H.*, et al.* An integrated instrument of DUV-IR photoionization mass spectrometry and spectroscopy for neutral clusters. *Rev. Sci. Instrum.* **90**, 073101 (2019).
34. Huang, W., Wang, L.-S. Au_{10}^-: Isomerism and structure-dependent O_2 reactivity. *Phys. Chem. Chem. Phys.* **11**, 2663−2667 (2009).
35. Lyalin, A., Taketsugu, T. Reactant-promoted oxygen dissociation on gold clusters. *J. Phys. Chem. Lett.* **1**,

1752−1757 (2010).
36. Huang, L., Liu, W., Hu, J., Xing, X. Adsorption and activation of O_2 on small gold oxide clusters: The reactivity dominated by site-specific factors. *J. Phys. Chem. A* **126**, 5594−5603 (2022).
37. Schriver, K. E., Persson, J. L., Honea, E. C., Whetten, R. L. Electronic shell structure of group-iiia metal atomic clusters. *Phys. Rev. Lett.* **64**, 2539−2542 (1990).
38. Lin, Z., Kanters, R. P. F., Mingos, D. M. P. Closed-shell electronic requirements for condensed clusters of the group 11 elements. *Inorg. Chem.* **30**, 91−95 (1991).
39. Martin, T. P., Bergmann, T., Gdhlich, H., Lange, T. Shell structure of clusters. *J. Phys. Chem.* **95**, 6421-6429 (1991).
40. Nygren, M. A., Siegbahn, P. E. M., Jin, C., Guo, T., Smalley, R. E. Electronic shell closings in metal cluster plus adsorbate systems: Cu_7^+CO and Cu_{17}^+CO. *J. Chem. Phys.* **95**, 6181−6184 (1991).
41. Pekka, P. Strong closed-shell interactions in inorganic chemistry. *Chem. Rev.* **97**, 597−636 (1997).
42. Luo, Z., Gamboa, G. U., Smith, J. C., Reber, A. C., Reveles, J. U., Khanna, S. N.*, et al.* Spin accommodation and reactivity of silver clusters with oxygen: The enhanced stability of Ag_{13}^-. *J. Am. Chem. Soc.* **134**, 18973−18978 (2012).
43. Häkkinen, H., Yoon, B., Landman, U., Li, X., Zhai, H.-J., Wang, L.-S. On the electronic and atomic structures of small Au_n^- (n = 4−14) clusters: a photoelectron spectroscopy and density-functional study. *J. Phys. Chem. A* **107**, 6168−6175 (2003).
44. Zhao, J., Shi, R., Sai, L., Huang, X., Su, Y. Comprehensive genetic algorithm forab initioglobal optimisation of clusters. *Mol. Simul.* **42**, 809−819 (2016).
45. Frisch, M. J., Trucks, G. W., Schlegel, H. B., Scuseria, G. E., Robb, M. A., Cheeseman, J. R.*, et al. Gaussian 16 rev. B.01*. Gaussian, Inc.: Wallingford, CT, 2016.
46. Zhao, Y., Su, J., Gong, Y., Li, J., Zhou, M. Noble-gas-induced disproportionation reactions: Facile superoxo-to-peroxo conversion on chromium dioxide. *J. Phys. Chem. A* **112**, 8606−8611 (2008).
47. Citra, A., Wang, X., Andrews, L. Reactions of laser-ablated gold with nitric oxide: Infrared spectra and DFT calculations of AuNO and $Au(NO)_2$ in solid argon and neon. *J. Phys. Chem. A* **106**, 3287−3293 (2002).
48. Ma, J., Wang, T., Yang, J., Hu, J., Xing, X. Adsorption and reactions of NO molecules on anionic gold clusters in the size range below 1 nm: Effects of clusters' global electronic properties. *Phys. Chem. Chem. Phys.* **22**, 25227−25235 (2020).
49. Hu, F., Yang, G., Zheng, L.-M., Liang, G.-J., Wang, Q.-M. Deciphering icosahedra structural evolution with atomically precise silver nanoclusters. *Science* **389**, 921−924 (2025).
50. Du, Q., Wu, X., Wang, P., Wu, D., Sai, L., King, R. B.*, et al.* Structure evolution of transition metal-doped gold clusters $M@Au_{12}$ (M = 3d–5d): Across the periodic table. *J. Phys. Chem. C* **124**, 7449−7457 (2020).
51. Dolg, M., Wedig, U., Stoll, H., Preuss, H. Energy-adjusted ab initio pseudopotentials for the first row transition elements. *J. Chem. Phys.* **86**, 866−872 (1987).
52. Reed, A. E., Weinstock, R. B., Weinhold, F. Natural population analysis. *J. Chem. Phys.* **83**, 735−746 (1985).
53. Lu, T., Chen, F. Multiwfn: A multifunctional wavefunction analyzer. *J. Comput. Chem.* **33**, 580−592 (2012).
54. Bader, R. F. W., Carroll, M. T., Cheeseman, J. R., Chang, C. Properties of atoms in molecules: Atomic volumes. *J. Am. Chem. Soc.* **109**, 7968−7979 (1987).
55. Liu, Z., Lu, T., Chen, Q. Intermolecular interaction characteristics of the all-carboatomic ring, cyclo[18]carbon: Focusing on molecular adsorption and stacking. *Carbon* **171**, 514−523 (2021).
56. Humphrey, W., Dalke, A., Schulten, K. VMD: Visual molecular dynamics. *J. Mol. Graph.* **14**, 33−38 (1996).

Methods

Experimental methods

The instrumental setup employed in this work to acquire the research findings is based on self-designed equipment described in prior publications[33]. The experiments used a laser vaporization source with a gold disc target. A 532 nm laser beam struck the target surface, and a pulsed valve introduced high-purity helium carrier gas (99.999%, 10 atm) to entrain the resulting plasma. The plasma cooled before being injected into a growth chamber and passed through a supersonic nozzle (Φ = 2 mm, L = 35 mm), where cluster growth occurred. The generated clusters were collimated by a skimmer and detected using a custom high-resolution reflection time-of-flight mass spectrometer (Re-TOFMS). Cluster size distribution was controlled by adjusting the laser Q-switch delay and carrier gas pulse width. The Re-TOFMS system comprised a pulsed acceleration

field and a constant-voltage DC reflectron field, with product mass numbers determined from time-of-flight differences of ions with distinct mass-to-charge ratios.

For reaction studies, reactant gases were introduced into the growth chamber through a pulsed valve to react with the clusters. The resulting products were then carried by the carrier gas to the detection chamber for mass spectrometry analysis. By adjusting the pulse width of the carrier gas, different reactant concentrations could be achieved, enabling controlled reactions of size-dependent gold clusters. When the reactant gas concentration was low, the reactions of these gold clusters were treated as pseudo-first-order processes, from which the rate constants for their reactions with O_2 and NO were determined.

DFT calculation method

Unbiased global structure searches for Au_n^- clusters ($n = 7-20$) are performed via a comprehensive genetic algorithm (CGA)[44] implemented in the DMol^3 package. For each cluster size, an initial population of sixteen randomly constructed geometries is adopted. In every evolutionary generation, new candidate structures are generated by crossover and mutation operations, each assigned an equal probability of 50%. A maximum of 5000 iteration steps is employed to guarantee convergence to the global minimum structure. All candidate configurations are further optimized at the DFT level using the all-electron relativistic approach with the PBE functional and DND basis set.

Low-energy isomers screened by the CGA method are further reoptimized with the Gaussian 16 program package[45]. The revTPSS functional together with the SDD basis set is adopted for Au atoms, whose reliability has been validated in our previous studies[50]. For the interactions of Au_n^- clusters with O_2 and NO, all plausible adsorption sites—including top, bridge, and hollow sites—are fully considered. Both singlet and triplet spin states are evaluated for even-electron systems. The 6-311+G(*d*) basis set is applied to N and O atoms[51]. The HOMOs and LUMOs are also calculated with hybrid functional at the PBE0/SDD level of theory. Atomic charge distributions are obtained via natural population analysis (NPA)[52]. Electron density surfaces (EDSs) are calculated using the Multiwfn code[53-55]. All molecular structure graphics are visualized and rendered by VMD software[56].

GCSS model theory

We represented each delocalized electron as an independent particle confined to a domain Ω and solved the stationary Schrödinger equation with the bare electron mass m_e:

$$\begin{gathered}\widehat{H}\psi_i(\vec{r}) = \left[-\frac{\hbar^2}{2m_e}\nabla^2 + V_\Omega(\vec{r})\right]\psi_i(\vec{r}) = E_{phys_i}\psi_i(\vec{r}) \\ V_\Omega(\vec{r}) = \begin{cases} 0 & if\ \vec{r} \in \Omega \\ +\infty & if\ \vec{r} \notin \Omega \end{cases}\end{gathered} \tag{1}$$

The infinite barrier imposes a homogeneous Dirichlet boundary condition. The domain is defined either by an analytical geometry, Ω_g, rasterized by an interior-exterior mask, or directly from a DFT electron-density cube (Ω_ρ). In the latter case, the density threshold is supplied explicitly or taken as the median cube density interpolated at the Multiwfn surface vertices:

$$\psi_i(\vec{r})|_{\vec{r}\in\partial\Omega} = 0,\ \Omega = \Omega_g,\ \text{or}\ \Omega_\rho = \{\vec{r}: \rho(\vec{r}) \geq \rho_{\text{iso}}\} \tag{2}$$

For Cartesian-grid solvers, the negative Laplacian was discretized on retained nodes by second-order central differences with spacings dx, dy, and dz. All six diagonal contributions were retained, while missing neighbours were assigned zero ghost values, imposing the Dirichlet condition on the voxelized boundary. Axisymmetric ellipsoids instead used sectorwise cylindrical generalized eigenproblems, $K\mathrm{u} = \lambda M\mathrm{u}$:

$$\begin{aligned} A\mathrm{c}_i = \lambda_i \mathrm{c}_i, (Ac)_{ijk} = 2(dx^{-2} + dy^{-2} + dz^{-2})c_{ijk} \\ -dx^{-2}(\tilde{c}_{i-1,j,k} + \tilde{c}_{i+1,j,k}) \\ -dy^{-2}(\tilde{c}_{i,j-1,k} + \tilde{c}_{i,j+1,k}) \\ -dz^{-2}(\tilde{c}_{i,j,k-1} + \tilde{c}_{i,j,k+1}). \end{aligned} \tag{3}$$

The lowest eigenpairs were obtained with sparse eigensolvers. Cartesian eigenvectors for overlaps, projections, and symmetry analysis were Euclidean orthonormal on retained nodes. On a uniform grid, the factor $(dx\,dy\,dz)^{-\frac{1}{2}}$ gives volume-normalized plotting wavefunctions for display, whereas cylindrical eigenvectors were M-normalized. Thus $|\psi_i|^2$ is a single-particle probability-density pattern, while signed isosurfaces retain phase. Idealized shapes were rescaled to a common volume, and energies were reported in equal-volume units E*,

$$\begin{aligned} E_i(\mathrm{E}^*) = E_{phys_i} \cdot \frac{2m_e R_0^2}{\pi\hbar^2} = \frac{k_i^2 R_0^2}{\pi} \\ R_0 = \left(\frac{3|\Omega|}{4\pi}\right)^{\frac{1}{3}} \\ k_i^2 = \frac{\lambda_i}{a_{eq}^2} \text{ for a unit-edge well} \end{aligned} \tag{4}$$

Here, $R_0 = (\frac{3|\Omega|}{4\pi})^{\frac{1}{3}}$ is the equal-volume sphere radius; voxel masks use $|\Omega| \approx N_{\mathrm{in}}\, dx\, dy\, dz$. On density grids, $\lambda_i = k_i^2$; for unit-edge wells, $k_i^2 = \frac{\lambda_i}{a_{\mathrm{eq}}^2}$. In a sphere, n and l are exact and follow from the zeros of the spherical Bessel functions. For a non-spherical well, each numerical eigenstate ψ_{i} was assigned a parent (n_i, l_i) shell by maximum projection onto the same-grid spherical-Bessel and real-spherical-harmonic reference subspace Φ_{nl}. Where implemented, a multiplet Ψ_g of dimension d_g was assigned a parent shell by maximizing its dimension-normalized subspace projection:

$$(n,l)_g = \underset{n,l}{\mathrm{argmax}} \frac{\|\Phi_{nl}^{\dagger}\Psi_g\|_F^2}{d_g}. \tag{5}$$

Parent-shell rules were solver specific: ellipsoidal branches were followed from the spherical limit; T_d and O_h combined subspace weights with energetic and symmetry compatibility; I_h used the largest subspace weight; and density-cube calculations used basis-dependent statewise labels. The C_{3v} and D_{3h} scripts omitted spherical-parent projection. Grouped T_d, O_h, I_h, and density-derived states were classified through operation traces and character tables, whereas C_{3v} and D_{3h} states used rotation and mirror overlaps. Density-derived blocks were additionally assessed by character mismatch and subspace leakage, with heuristic subdivision when appropriate.

These thresholds are numerical acceptance criteria, and both parent-shell and irreducible-representation labels are symmetry-supported numerical descriptors rather than exact quantum numbers. Full equations, decomposition criteria and group-specific sampling procedures are provided in the Supplementary Information. Further details regarding the GCSS model are available in the MATLAB codes deposited on Zenodo (DOI: 10.5281/zenodo.22127728).

Supplementary Files

This is a list of supplementary files associated with this preprint. Click to download.

- GCSSESImaterials20261021.pdf